Short communication

Cobalt oxides nanoparticles supported on nitrogen-doped carbon nanotubes as high-efficiency cathode catalysts for microbial fuel cells

Wei Yang[a,b,c], Jia En Lu[c], Yudong Zhang[a,b], Yi Peng[c], Rene Mercado[c], Jun Li[a,b,*], Xun Zhu[a,b], Shaowei Chen[c,*]

[a] Key Laboratory of Low-grade Energy Utilization Technologies and Systems (Ministry of Education), Chongqing University, Chongqing 400030, China
[b] Institute of Engineering Thermophysics, School of Energy and Power Engineering, Chongqing University, Chongqing 400030, China
[c] Department of Chemistry and Biochemistry, University of California, 1156 High Street, Santa Cruz, California 95064, USA

GRAPHICAL ABSTRACT
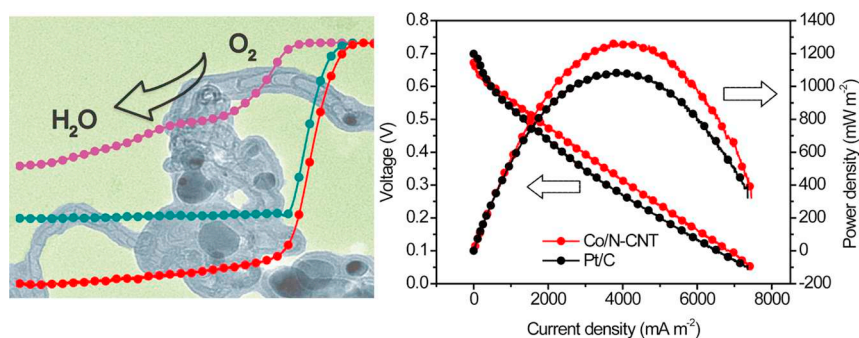
ARTICLE INFO

ABSTRACT

Microbial fuel cell is a unique energy technology where both wastewater treatment and electricity generation take place concurrently. However, the performance is typically rather limited due to the sluggish electron-transfer kinetics of oxygen reduction reaction at the cathode. Thus, development of high-performance cathode catalysts is of fundamental significance for the wide-spread application of microbial fuel cell. In this study, nanocomposites based on cobalt oxide nanoparticles supported on nitrogen-doped carbon nanotubes (Co/N-CNT) were synthesized by controlled pyrolysis of graphitic carbon nitride and cobalt acetate. Electrochemical tests indicated that the Co/N-CNT nanocomposites exhibited a high ORR electrocatalytic activity with a half-wave potential of $+0.82\,V$ and onset potential of $+0.91\,V$ vs. RHE, mostly via a four-electron reduction pathway. This was ascribed to the formation of high-efficiency Co—N active sites that facilitated the ORR kinetics. A microbial fuel cell using the as-prepared Co/N-CNT as the cathode catalyst achieved a maximum power density of $1260\,mW\,m^{-2}$, which was 16.6% higher than that based on state-of-art Pt/C catalyst ($1080\,mW\,m^{-2}$). The results suggest that Co/N-CNT nanocomposites may serve as viable cathode catalysts in microbial fuel cell application.

* Corresponding authors.
  E-mail addresses: lijun@cqu.edu.cn (J. Li), shaowei@ucsc.edu (S. Chen).

1. Introduction

Microbial fuel cell (MFC) has been attracting extensive attention lately because it can degrade organic pollutants in wastewater and concurrently produce electricity using anode bacteria [1–4]. Of these, MFC with an air cathode is a promising design for practical utilization, due to the direct use of freely available oxygen in the air as electron acceptors [5–7]. Nevertheless, despite substantial progresses in recent years, the power density of MFC has remained relatively low, primarily due to the high overpotential and sluggish electron-transfer kinetics of oxygen reduction reaction (ORR) at the cathode [8,9]. This is a major limitation hindering the practical application of MFC. Platinum (Pt)-based nanoparticles have been used extensively as the catalysts of choice for ORR; yet the high cost, low earth abundance, and low poison tolerance in the presence of contaminants in wastewater have been detrimental to the device performance and applications [10,11]. Within this context, a range of non-precious metal/carbon nanocomposites have been prepared by using select organometallic complexes as precursors, such as iron(II) phthalocyanine and cobalt tetra-methoxyphenylporphyrin, and exhibited rather remarkable electro-catalytic performance as the air cathode catalysts of MFC [12,13]. In fact, carbon-supported non-precious metal-based catalysts have been proposed as viable alternatives as cathode catalysts for MFC, because of their low costs, high natural abundance, apparent catalytic activity, and good mechanical strength [9,14–23]. For nitrogen-doped carbon, metal-nitrogen coordination (MN_x) moieties are typically formed within the carbon matrix (M-N-C) and serve as the ORR active sites [10,24,25]. For instance, an MFC using Fe,N-codoped carbon as the cathode catalyst has been found to deliver a maximum power density (P_{max}) of $3118.9 \, mW \, m^{-2}$, which is markedly higher than that obtained with a Pt/C cathode ($2017.6 \, mW \, m^{-2}$) under the same operating conditions [14].

In general, the preparation of M-N-C hybrids entails two steps, synthesis of the carbon substrates, such as graphene and carbon nanotubes, followed by controlled pyrolysis after the addition of select nitrogen-containing precursors to facilitate N doping (e.g., HNO_3, NH_3, and urea) and metal salts to incorporate metal dopants. Graphitic carbon nitride (C_3N_4) represents a unique precursor. It is a conjugated organic semiconductor consisting of sp^2 hybridized nitrogen and carbon atoms [26], where the abundant pyridinic nitrogen moieties can be exploited for the coordination of transition metal centers [27,28].

Herein, we demonstrate that Co,N-codoped carbon nanotubules can be synthesized pyrolytically by using cobalt acetate as the cobalt precursor and C_3N_4 as the carbon and nitrogen sources. The structures of the resulting Co/N-CNT nanocomposites were characterized by X-ray diffraction (XRD), X-ray photoelectron spectroscopy (XPS) and Raman measurements. Electrochemical tests showed that the Co/N-CNT nanocomposites exhibited a high ORR electrocatalytic activity with a half-wave potential of +0.82 V and onset potential of +0.91 V vs. RHE, mostly via a four-electron reduction pathway. This was ascribed to the high efficiency of Co−N active sites that facilitated the ORR kinetics. Furthermore, the performance of the resulting Co/N-CNT nanocomposites as MFC air cathode catalysts was examined in a home-made MFC, which achieved a maximum power density of $1260 \, mW \, m^{-2}$, 16.6% higher than that based on a state-of-art Pt/C catalyst ($1080 \, mW \, m^{-2}$). These results suggest that Co/N-CNT nanocomposites may serve as viable ORR catalysts in MFC applications.

2. Experimental section

2.1. Synthesis of C_3N_4

C_3N_4 was prepared by direct pyrolysis of melamine under ambient condition, as described previously [28]. In brief, melamine (8 g) was placed in a crucible and the temperature was increased to 600 °C at the heating rate of 2.3 °C min^{-1}. The sample was heated at 600 °C for 2 h

and then cooled down to room temperature. The yellow product was collected, ground into powders, and dispersed in water under sonication overnight to produce C_3N_4 nanosheets.

2.2. Synthesis of cobalt, nitrogen codoped carbon nanotube

In a typical experiment, 50 mg of the C_3N_4 powders prepared above was dispersed in 50 mL of Nanopure water and sonicated overnight, into which was then added 0.319 g of cobalt(II) acetate (Co$(OAc)_2·4H_2O$). The solution was refluxed at 100 °C for 30 min. The pH of the mixture was then adjusted to ~12 by using a 0.1 M NaOH solution, and the dispersion was refluxed for another 30 min. The precipitate was collected by centrifugation at 4500 rpm for 10 min. The obtained product was dried at 80 °C, and then the temperature was increased to 800 °C at the heating rate of 5 °C min^{-1}, where pyrolysis was performed for 2 h, affording Co,N-codoped carbon nanotubes that were denoted as Co/N-CNT.

2.3. Characterizations

The morphology of the samples was characterized by using a transmission electron microscope (TEM, Philips CM300 at 300 kV). The TEM samples were prepared by dropcasting a dilute dispersion of the samples in ethanol onto a TEM grid and dried in a vacuum oven. XRD patterns were acquired with a Rigaku Americas Miniflex Plus powder diffractometer operated at 40 kV and 30 mA. Raman spectra were acquired on a LabRAM HR Evolution using an Ar ion laser at the excitation wavelength of 514.5 nm. XPS measurements were conducted using a PHI 5400/XPS instrument equipped with an Al K_α source operated at 350 W and 10^{-9} Torr.

2.4. Electrochemistry

Electrochemical tests were carried out on a CHI710 workstation and electrochemical impedance spectra were collected with a Gamry Reference 600 instrument. A Ag/AgCl (1 M KCl) and a graphite rod were used as the reference and counter electrode, respectively, while a rotating (golden) ring–(glassy carbon) disk electrode (RRDE, from Pine Instrument) was used as the working electrode. The Ag/AgCl electrode was calibrated against a reversible hydrogen electrode (RHE) and all potentials in the present study were referenced to this RHE. To prepare catalyst inks, 5 mg of the as-prepared catalysts (or 5 mg of commercial Pt/C, 20 wt%) were dispersed in 2 mL of a water/ethanol (v:v 1:2) mixture along with 10 mL of a Nafion solution, and the mixture was sonicated for at least 30 min to achieve good dispersion of the materials. Then 20 μL of the above inks was dropcast onto the clean surface of the glassy carbon electrode and dried at room temperature, corresponding to a catalyst loading of 0.203 mg cm^{-2}. Prior to use, the RRDE was polished with 50 nm Al_2O_3 powders and washed extensively with Nanopure water.

The RRDE tests were conducted in nitrogen-sparged 0.1 M NaOH and then switched to an oxygen-saturated NaOH solution. During the tests, the potential of the working electrode was scanned from +1 to 0 V vs. RHE at the potential sweep rate of 10 mV s^{-1} with the rotation rate varied from 400 to 2500 rpm. The current acquired in the nitrogen-saturated solution was subtracted from that in oxygen-sparged solution to obtain the ORR current. The number of electron transfer (n) and yield of hydrogen peroxide (H_2O_2%) were calculated based on the following equations,

$$n = \frac{4i_{disk}}{i_{disk} + i_{ring}/N_r} \tag{1}$$

$$H_2O_2\% = \frac{200i_{ring}/N_r}{i_{disk} + i_{ring}/N_r} \tag{2}$$

where i_{disk} is the disk current, i_{ring} is the ring current due to the

oxidation of hydrogen peroxide, and N_r is the collection efficiency of the gold ring (0.4).

2.5. Assembly and set-up of MFCs

To construct an MFC, air cathodes were prepared by coating a catalyst layer onto teflonized carbon cloth (WOS 1002 PHYCHEMi Co. Ltd., China) at a catalyst loading of $2 \, mg \, cm^{-2}$ for Co/N-CNT and $0.5 \, mg \, cm^{-2}$ Pt/C. In brief, the carbon cloth was teflonized by brushing four layers of polytetrafluoroethylene (60 wt% solution, Sigma Aldrich) on one side and thermally treated at 370 °C for 20 min. The prepared catalyst ink was then dropcast onto the other side of the teflonized carbon cloth and dried at 80 °C for 1 h. Carbon cloth was directly used as anode after washing in acetone. The surface area of both the anode and cathode was $7 \, cm^2$. The resulting anode and air cathode were mounted onto the two sides of a cubic MFC with a cylindrical chamber (a volume of 28 mL with 3 cm diameter, and 4 cm spacing between the anode and cathode). The MFC was inoculated with anaerobic digester sludge containing exoelectrogenic bacteria. During the inoculation process, an external resistor of $1000 \, \Omega$ was connected to the MFC. The MFC was operated in the fed-batch mode at room temperature $(30 \pm 1 \, °C)$. Anolyte was replenished with a fresh medium when the cell voltage fell below 50 mV. The fresh medium was composed of $2.04 \, g \, L^{-1}$ sodium acetate, $11.82 \, g \, L^{-1}$ Na_2HPO_4, $2.32 \, g \, L^{-1}$ KH_2PO_4, $0.1 \, g \, L^{-1}$ NH_4Cl, $0.5 \, g \, L^{-1}$ NaCl, $0.1 \, g \, L^{-1}$ $MgSO_4 \cdot 7H_2O$, $15 \, mg \, L^{-1}$ $CaCl_2 \cdot 2H_2O$ and $1.0 \, mL \, L^{-1}$ trace elements [29].

The power density and cell voltage were evaluated by linear sweep voltammetric (LSV) measurements in the potential range between open circuit voltage (OCV) and 50 mV at the potential scan rate of $0.2 \, mV \, s^{-1}$. The cathode was the working electrode, and the anode was connected to the counter and reference electrodes. The power density and current density was normalized to the projected surface of cathode $(7 \, cm^2)$.

3. Results and discussion

Fig. 1 shows the representative TEM images of the as-obtained Co/N-CNT nanocomposites. One can see that the sample consisted of a number of bamboo-like hollow carbon nanotubes, with a length up to a few hundred nm, an outer diameter of 15–30 nm and a wall thickness of ca. 5 nm (Fig. 1a,b) [30]. The formation of bamboo-like carbon nanotubes was probably due to the presence of pentagon structures in the graphite network caused by nitrogen doping [31]. These nanotubes were also decorated with dark-contrast nanoparticulate objects with a diameter of 15–30 nm (marked by red circles in Fig. 1c) that were most likely CoO_x nanoparticles. The nanoparticles were encapsulated within discontinuous graphite layers, which displayed an interplanar distance of 0.347 nm that was consistent with the (210) planes of graphitic carbon [32].

The XRD patterns of the obtained samples are shown in Fig. 2a. A main peak can be identified at 26.5° for Co/N-CNT, corresponding to the diffraction of the (002) crystalline planes of the graphitic carbon
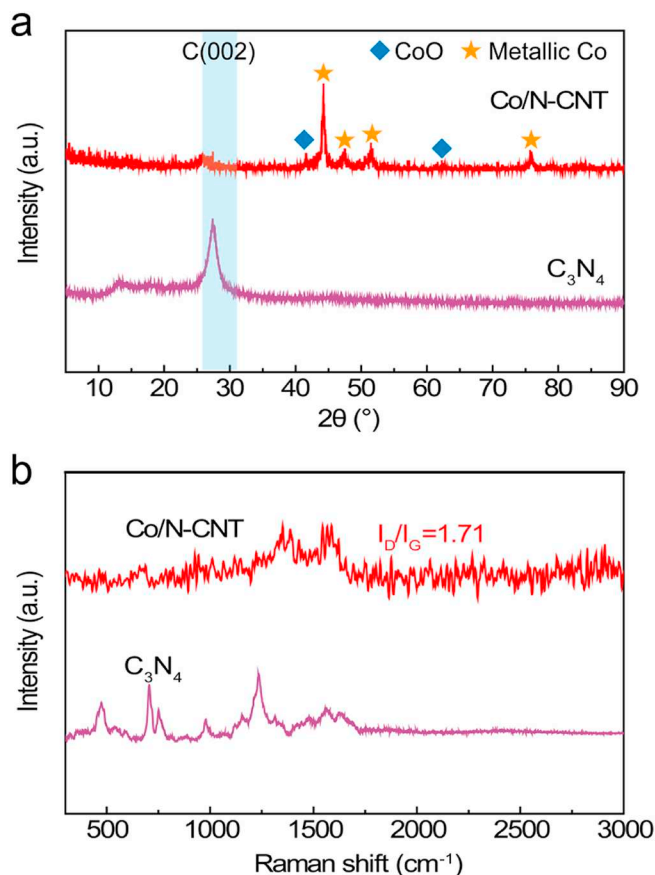

Fig. 2. (a) XRD and (b) Raman spectra of Co/N-CNT and C_3N_4.

frameworks [32]. For comparison, C_3N_4 showed a diffraction peak at a somewhat higher angle of 27.5°, characteristic of its (002) planes [27,28]. These results suggest effective conversion of C_3N_4 into graphitic carbon skeletons by pyrolytic treatments. Several additional diffraction peaks can also be seen at 44.3°, 51.5° and 75.8° that are consistent with the (111), (200), and (220) planes of metallic Co (PDF# 15-0806) [33], whereas the peak at 47.5° likely arose from the (100) planes of hexagonal centered (hcp) cobalt (PDF# 5-0727) [34]. In addition, the small peaks at 41.7° and 61.5° are likely due to the (200) and (220) diffractions of CoO (PDF# 48-1719) [35]. This suggests the formation of CoO_x supported in a carbon matrix. Further structural insights were obtained by Raman measurements (Fig. 2b). It is found that C_3N_4 exhibited four characteristic vibrations at ca. 472, 712, 980 and $1226 \, cm^{-1}$ [36], whereas for Co/N-CNT, two major peaks can be identified at ca. $1352 \, cm^{-1}$ and $1580 \, cm^{-1}$, due to the D and G bands of graphitic carbons [37], and the ratio of the band intensity (I_D/I_G) was estimated to be 1.71, indicative of a moderately defective structure of the carbon scaffolds.
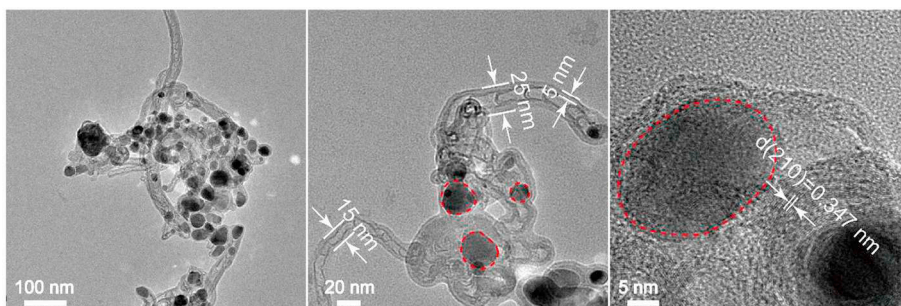

Fig. 1. Representative TEM images of Co/N-CNT at different magnifications. Scale bars are (a) 100 nm, (b) 20 nm and (c) 5 nm.
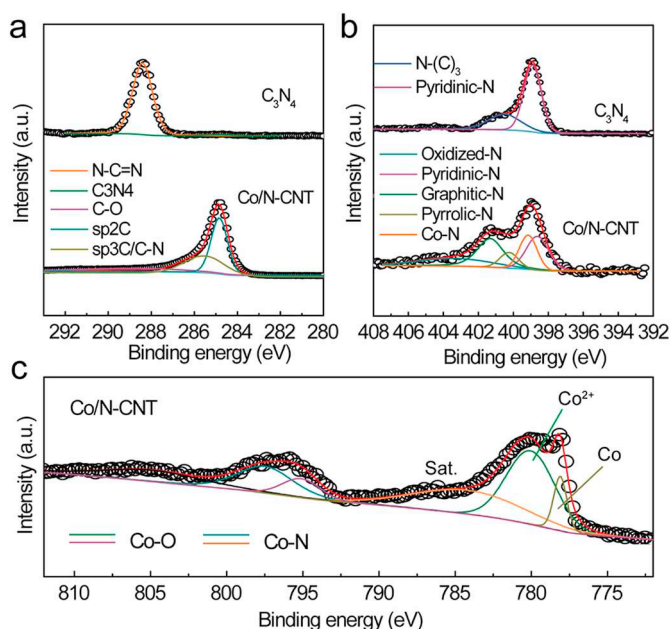
Fig. 3. High-resolution XPS scans of the (a) C 1s, (b) N 1s and (c) Co 2p electrons of Co/N-CNT and C_3N_4. Black circles are experimental data and colored curves are deconvolution fits.

XPS analysis was then conducted to evaluate the chemical composition and valence states of the nanocomposites. Fig. 3a depicts the C 1s spectra of Co/N-CNT and C_3N_4. It can be seen that C_3N_4 exhibited a peak at 288.4 eV, which can be assigned to the sp^2-hybridized carbon in the N—C=N ring [27,28]. For the Co/N-CNT sample, the C 1 s spectrum can be deconvoluted into three subpeaks at 284.8, 285.53 and 288.8 eV, due to sp^2 C, sp^3 C/C—N, and C=O, respectively [10]. In Fig. 3b, the N 1s spectrum of C_3N_4 was deconvoluted into two subpeaks at 398.9, and 400.5 eV, corresponded to the pyridinic-N and N—$(C)_3$, respectively [27,28], whereas for the Co/N-CNT sample, three subpeaks can be resolved at 398.4, 401.0, and 399.9 eV, corresponding to the pyridinic-N, graphitic-N and pyrrolic-N, respectively. Two additional nitrogen species can also be identified at 403.3 and 399.1 eV, which can be ascribed to oxidized-N and N in Co—N moieties, respectively [38]. These indicate that indeed both Co and N species were incorporated into the carbon skeletons forming CoN_x moieties. The contents of these nitrogen dopants were then quantified, based on the integrated peak areas (Table S1). It can be seen that Co/N-CNT consisted of a pyridinic-N content of 1.37 at.% and graphitic-N of 1.61 at.%. Fig. 3c shows the Co 2p spectrum of Co/N-CNT. One can see that the sample exhibited three pairs of peaks. The first doublet can be identified at ~778 and 794 eV due to metallic Co, and another at 781 and 796 eV to Co^{2+} in CoO, whereas the peaks at 785 and 802 eV are the satellites [39], in good agreement with results from XRD measurements (Fig. 2a). In addition, the Co content in Co/N-CNT was estimated to be 2.82 at.%.

The electrochemical activity of the obtained catalysts was then evaluated in a typical three-electrode configuration in 0.1 M NaOH. From Fig. 4a, it can be seen that with an oxygen-saturated electrolyte solution, a cathodic peak appeared at +0.8 V, in contrast to the featureless response when the electrolyte was purged with N_2, indicating apparent ORR activity of the Co/N-CNT sample. The ORR activity was then tested in RDE measurements. From Figs. 4b and S1, one can see that the current density reached a plateau at potentials more negative than +0.7 V and increased with increasing rotation rates. At 1600 rpm, the half-wave potential ($E_{1/2}$) can be identified at +0.84 V for Pt/C, +0.82 V for Co/N-CNT, and +0.64 V for C_3N_4, with the corresponding onset potential (E_{onset}) at +0.93, +0.91, and +0.76 V, respectively (Fig. 4c). That is, the performance of Co/N-CNT was higher than that of C_3N_4, and close to that of Pt/C. It should be noted that the $E_{1/2}$

(+0.82 V) of Co/N-CNT is actually more positive than or comparable to those of relevant nitrogen-doped carbon supported cobalt oxide catalysts reported in recent literature (Table S2), demonstrating the remarkable activity of the as-prepared Co/N-CNT composite. This high activity probably arose from the formation of Co-N species, as manifested in XPS measurements (Fig. 3), that have been argued to be the active sites for ORR, with additional contributions from select N dopants such as pyridinic-N and graphitic-N [38].

The number of electron transfer (n) was then evaluated according to eq. (1), which was over 3.4, suggesting that ORR proceeded mainly via the $4e^-$ pathway on Co/N-CNT. In fact, at +0.6 V, the n value was 3.9 for Pt/C, 3.4 for Co/N-CNT, and 3.1 for C_3N_4. The slightly lower n value of Co/N-CNT than that of Pt/C suggests a somewhat higher yield of H_2O_2 during the ORR process (Fig. S2). From the practical point of view, the high half-wave potential and high limiting current of Co/N-CNT ensure an efficient ORR performance, and the slightly higher H_2O_2 yield by Co/N-CNT might actually provide an additional benefit to inhibit the formation of biofilms on the cathode surface, as compared to Pt/C [40,41].

The ORR kinetics and the effective electrochemical surface area (ECSA) of catalysts are then evaluated. The Tafel plot was obtained by using the linear segments of the LSV curves, as shown in Fig. 5a. It can be seen that the Pt/C, Co/N-CNT, and C_3N_4 show a Tafel slope of 88, 74, and 100 mV dec^{-1}, respectively. In addition, from the Koutecky-Levich plot in Fig. 5b, the kinetic current density (J_K) at +0.6 V can be estimated to be 16.29 mA cm^{-2} for Pt/C, 23.05 mA cm^{-2} for Co/N-CNT, and 2.15 mA cm^{-2} for C_3N_4. With the lowest Tafel slope and highest J_K, Co/N-CNT stood out as the best ORR catalyst among these samples. Consistent results were obtained with the comparison of ECSA among the catalysts, which can be represented by the electrode double-layer capacitance (C_{dl}). As shown in Fig. 5c,d, C_{dl} can be estimated by linear regression of the (non-faradaic) current vs. potential scan rate at 4.27×10^{-3} mF cm^{-2} for Co/N-CNT, about an order of magnitude higher than that (0.48×10^{-3} mF cm^{-2}) for C_3N_4 (Fig. S3). Electrochemical impedance measurements were then performed to evaluate the corresponding charge-transfer resistance (R_{ct}) under open circuit potential, as shown in Fig. 5e. The Nyquist plots were fitted based on the equivalent circuit (Fig. S4), with the fitting results summarized in Table S3. One can see that R_{ct} was only 23.4 Ω for Co/N-CNT, over three hundred times lower than that (7829 Ω) for C_3N_4 [28].

Stability and poison tolerance of catalysts are additional important factors affecting the practical application of MFC. In wastewater and activated sludge, a variety of sulfur-related pollutants are generally present, which can poison catalyst active sites and degrade the MFC performance [11]. In the present study, the stability and poisoning tests were conducted using S^{2-} as the poisoning species. As shown in Fig. 5f, chronoamperometric tests at +0.7 V show that the current response of the Co/N-CNT catalyst remained stable for over 1 h, whereas a 5% decrease was observed with Pt/C, indicating enhanced stability of Co/N-CNT. In addition, when 5 mM L^{-1} S^{2-} was added into the electrolyte, 93% of the current was retained with Co/N-CNT, significantly higher than that (44%) for Pt/C, indicating markedly enhanced poison tolerance. The higher poison tolerance of Co/N-CNT catalysts was probably due to the weak absorption of poison species, due to a relatively lower spin density on active sites, as compared to Pt [10].

The application of Co/N-CNT as the air cathode of MFC was then examined, in comparison with Pt/C. As shown in Fig. 6a, the cell performance was first tested based on polarization curves. It is obvious that the cell voltages of both MFCs decrease with the increase of current densities, and the MFC based on Co/N-CNT air cathode exhibited a higher cell voltage at current densities higher than 400 mA m^{-2}, indicating a higher power output than that with Pt/C. Indeed, it can be seen that the former MFC delivered a P_{max} of 1260 mW m^{-2}, which is 16.7% higher than that of the latter (1080 mW m^{-2}). The catalytic current of cathodes was also evaluated based on LSV tests, as shown in Fig. 6b. One can see that the Co/N-CNT cathode showed a higher
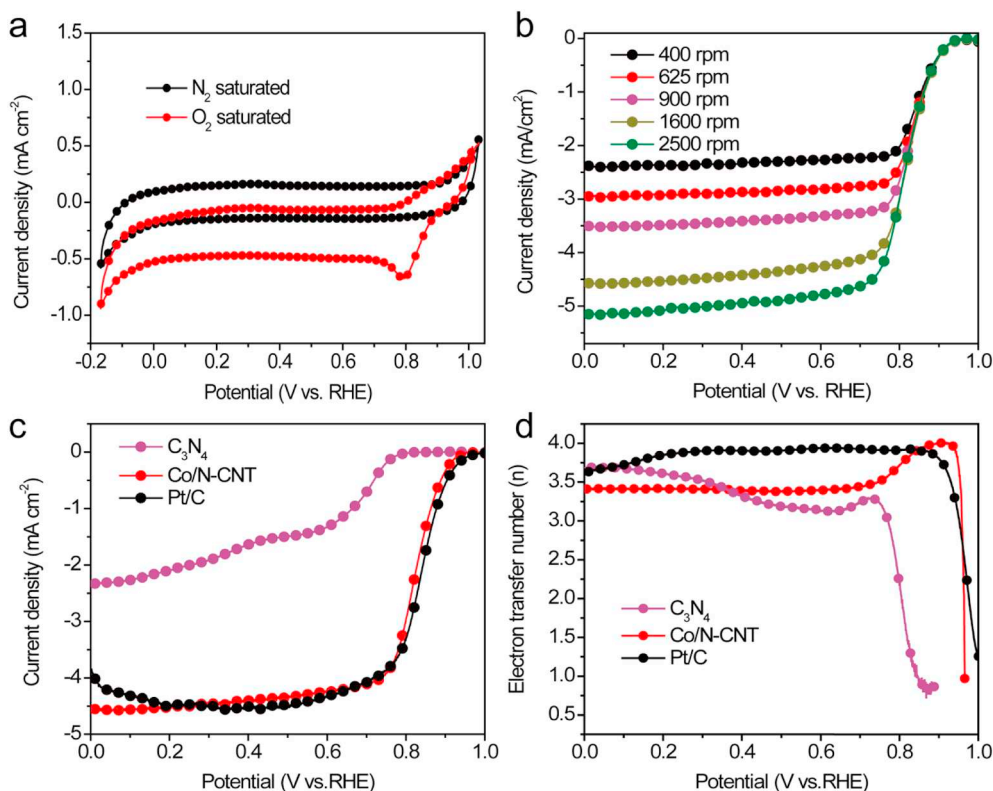
Fig. 4. (a) CV of Co/N-CNT in N_2 and O_2 saturated NaOH electrolyte, (b) LSV curves of Co/N-CNT at different rotating rates, (c) LSV curves of Co/N-CNT, C_3N_4 and Pt/C at the rotation rate of 1600 rpm, (d) number of electron transfer of Co/N-CNT, C_3N_4 and Pt/C.
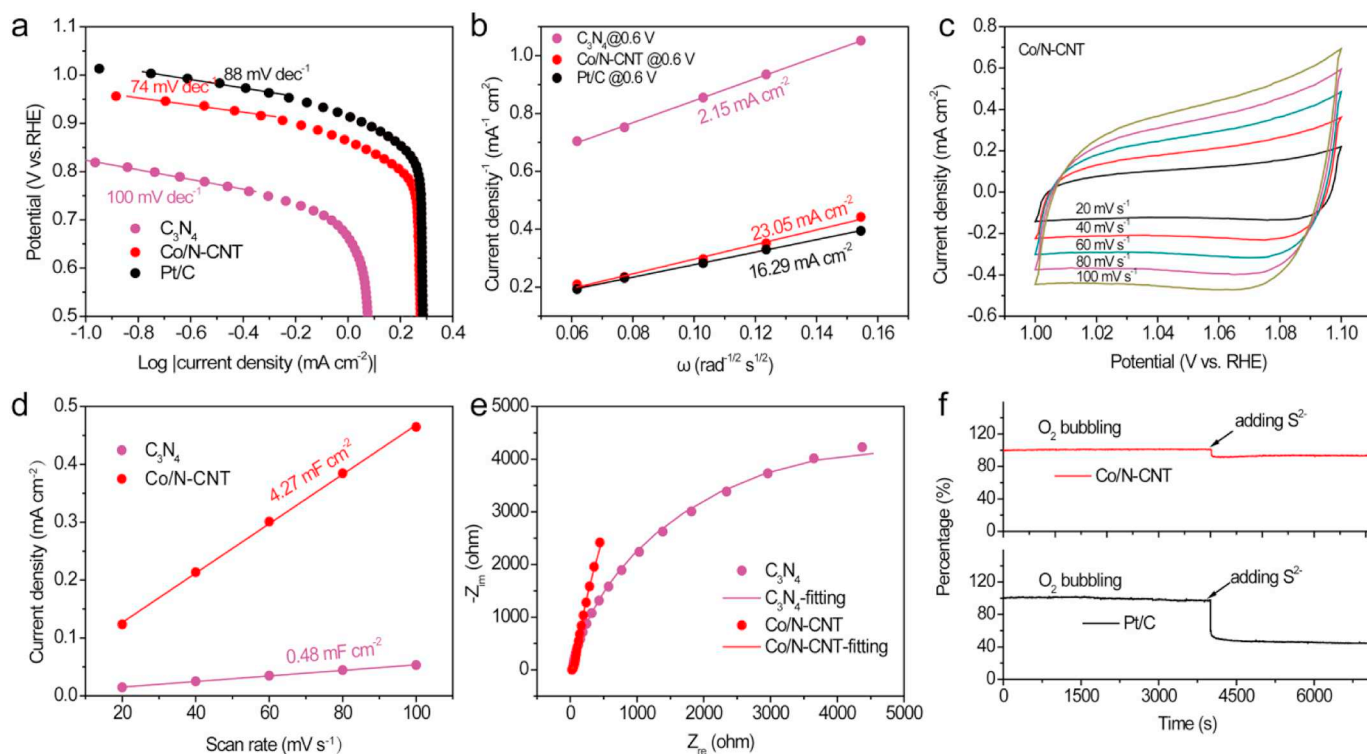

Fig. 5. (a) Tafel plots derived from LSV curves, (b) Koutecky-Levich plots of the catalyst samples at $+0.6$ V vs. RHE, (c) cyclic voltammograms within the range of $+1.0$ to $+1.1$ V vs. RHE, (d) variation of the double-layer charging currents at $+1.1$ V versus potential scan rate, (e) Nyquist plots of catalysts at the open circuit potential, (f) chronoamperometric responses of Co/N-CNT and Pt/C at the constant potential of $+0.7$ V vs. RHE before and after the addition of S^{2-} poisoning species.
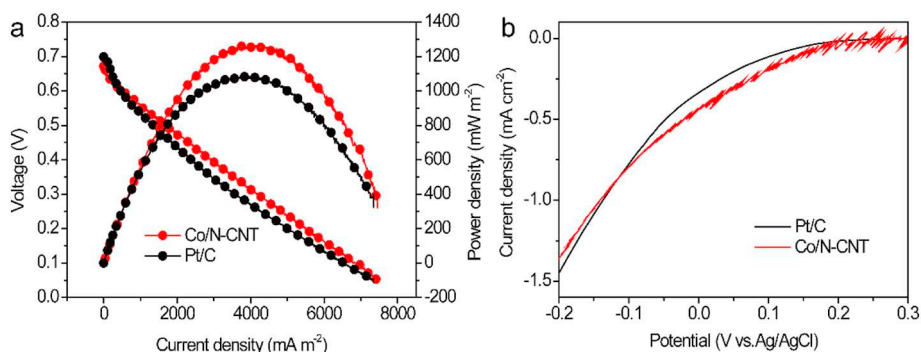
Fig. 6. (a) Polarization and power density curves and (b) LSV curves of MFC using Co/N-CNT and Pt/C as air cathode catalysts.

current response than Pt/C, suggesting a higher cathode performance under the MFC operation condition (current density $<$ 8000 mA m^{-2}). These results showed that the Co/N-CNT sample can be used as a viable ORR catalyst for MFC with a power output even higher than that of Pt/C.

It should be noted that the above MFC measurements were carried out in a neutral electrolyte solution, whereas the assessments of the electrocatalytic activity were performed in alkaline media (Fig. 4). This is because the ORR proceeds through the production of hydroxyl from oxygen and water in the cathodes even at neutral pH [42–44], such that the microenvironment in the catalyst layer of the air cathode tends to be very alkaline, in comparison to the neutral condition in the bulk solution. For instance, Yuan et al. [45] demonstrated that the pH near the air cathode surface could reach up to 11.6 $\pm$ 0.3 in the presence of a biofilm with a 100 Ω external resistance.

As the catalyst loading of air cathode varies greatly in the literature, it is difficult to directly compare the MFC performance with literature results. To give a reasonable comparison, we normalize the power density by the catalyst mass loading. The obtained mass specific power (MSP) was listed in Table S4. It can be seen that Co/N-CNT showed a high MSP of 63 W g^{-1}, one of the highest among leading results in the literature. The high MSP means that the cathode can use a low loading of catalyst to maintain a high power output in MFC operation, and hence a reduced cost of the device.

4. Conclusion

In this study, nitrogen-doped carbon nanotubes decorated with cobalt oxides nanoparticles (Co/N-CNT) were synthesized by a facile pyrolysis procedure. The prepared nanocomposites showed apparent electrocatalytic activity towards ORR, with a half-wave potential of $+0.82$ and onset potential of $+0.91$ V vs. RHE, respectively, highly comparable to that of Pt/C. This can be attributed to the high content of active Co−N sites, which facilitated ORR kinetics. The Co/N-CNT composite also showed enhanced stability and tolerance against poisoning species, as compared to Pt/C. Using Co/N-CNT as the air cathode catalyst, the corresponding MFC achieved a maximum power density of 1260 mW m^{-2}, which was 16.7% higher than that with a Pt/C cathode. These results show that the Co/N-CNT might serve as a high-efficiency ORR catalyst for MFC cathode.

Acknowledgements

Appendix A. Supplementary material

Supplementary data to this article can be found online at https://doi.org/10.1016/j.inoche.2019.04.036.

References

[1] J.R. Trapero, L. Horcajada, J.J. Linares, J. Lobato, Is microbial fuel cell technology ready? An economic answer towards industrial commercialization, Appl. Energy 185 (2017) 698–707.
[2] Y. Park, S. Park, V.K. Nguyen, J. Yu, C.I. Torres, B.E. Rittmann, T. Lee, Complete nitrogen removal by simultaneous nitrification and denitrification in flat-panel air-cathode microbial fuel cells treating domestic wastewater, Chem. Eng. J. 316 (2017) 673–679.
[3] L. He, P. Du, Y.Z. Chen, H.W. Lu, X. Cheng, B. Chang, Z. Wang, Advances in microbial fuel cells for wastewater treatment, Renew Sust Energy Rev 71 (2017) 388–403.
[4] J. Zhang, L.W. Li, J.L. Zheng, P.L. Yang, X.H. Wu, C.X. Cheng, J. Li, Y.J. Tian, F. Wang, Improved organic pollutants removal and simultaneous electricity production via integrating Fenton process and dual rotating disk photocatalytic fuel cell system using bamboo charcoal cathode, Chem. Eng. J. 361 (2019) 1198–1206.
[5] X.G. Song, J. Liu, Q. Jiang, Y.P. Qu, W.H. He, B.E. Logan, Y.J. Feng, Enhanced electricity generation and effective water filtration using graphene-based membrane air-cathodes in microbial fuel cells, J. Power Sources 395 (2018) 221–227.
[6] Z.J. Wang, G.D. Mahadevan, Y.C. Wu, F. Zhao, Progress of air-breathing cathode in microbial fuel cells, J. Power Sources 356 (2017) 245–255.
[7] Y. Park, S. Park, V.K. Nguyen, J.R. Kim, H.S. Kim, B.G. Kim, J. Yu, T. Lee, Effect of gradual transition of substrate on performance of flat-panel air-cathode microbial fuel cells to treat domestic wastewater, Bioresour. Technol. 226 (2017) 158–163.
[8] C. Cao, L.L. Wei, G. Wang, J.Q. Shen, In-situ growing NiCo2O4 nanoplatelets on carbon cloth as binder-free catalyst air-cathode for high-performance microbial fuel cells, Electrochim. Acta 231 (2017) 609–616.
[9] W. Yang, J. Li, D. Ye, X. Zhu, Q. Liao, Bamboo charcoal as a cost-effective catalyst for an air-cathode of microbial fuel cells, Electrochim. Acta 224 (2017) 585–592.
[10] B.Z. Lu, T.J. Smart, D.D. Qin, J.E. Lu, N. Wang, L.M. Chen, Y. Peng, Y. Ping, S.W. Chen, Nitrogen and iron-codoped carbon hollow nanotubules as high-performance catalysts toward oxygen reduction reaction: a combined experimental and theoretical study, Chem. Mater. 29 (2017) 5617–5628.
[11] C. Santoro, A. Serov, L. Stariha, M. Kodali, J. Gordon, S. Babanova, O. Bretschger, K. Artyushkova, P. Atanassov, Iron based catalysts from novel low-cost organic precursors for enhanced oxygen reduction reaction in neutral media microbial fuel cells, Energy Environ. Sci. 9 (2016) 2346–2353.
[12] F. Zhao, F. Harnisch, U. Schroder, F. Scholz, P. Bogdanoff, I. Herrmann, Application of pyrolysed iron(II) phthalocyanine and CoTMPP based oxygen reduction catalysts as cathode materials in microbial fuel cells, Electrochem. Commun. 7 (2005) 1405–1410.
[13] F. Zhao, F. Harnisch, U. Schröder, F. Scholz, P. Bogdanoff, I. Herrmann, Challenges and constraints of using oxygen cathodes in microbial fuel cells, Environ Sci Technol 40 (2006) 5193–5199.
[14] H. Tang, Y. Zeng, Y. Zeng, R. Wang, S. Cai, C. Liao, H. Cai, X. Lu, P. Tsiakaras, Iron-embedded nitrogen doped carbon frameworks as robust catalyst for oxygen reduction reaction in microbial fuel cells, Appl. Catal. B-Environ. 202 (2017)

550–556.

[15] X.-B. Gong, S.-J. You, X.-H. Wang, J.-N. Zhang, Y. Gan, N.-Q. Ren, A novel stainless steel mesh/cobalt oxide hybrid electrode for efficient catalysis of oxygen reduction in a microbial fuel cell, Biosens. Bioelectron. 55 (2014) 237–241.

[16] Z. Awan, K.S. Nahm, J.S. Xavier, Nanotubular MnO2/graphene oxide composites for the application of open air-breathing cathode microbial fuel cells, Biosens. Bioelectron. 53 (2014) 528–534.

[17] J. Huang, N. Zhu, T. Yang, T. Zhang, P. Wu, Z. Dang, Nickel oxide and carbon nanotube composite (NiO/CNT) as a novel cathode non-precious metal catalyst in microbial fuel cells, Biosens. Bioelectron. 72 (2015) 332–339.

[18] J. An, N. Li, L. Wan, L. Zhou, Q. Du, T. Li, X. Wang, Electric field induced salt precipitation into activated carbon air-cathode causes power decay in microbial fuel cells, Water Res. 123 (2017) 369–377.

[19] Y. Yang, T. Liu, Q. Liao, D. Ye, X. Zhu, J. Li, P. Zhang, Y. Peng, S. Chen, Y. Li, A three-dimensional nitrogen-doped graphene aerogel-activated carbon composite catalyst that enables low-cost microfluidic microbial fuel cells with superior performance, J. Mater. Chem. A 4 (2016) 15913–15919.

[20] L. Feng, Y. Yan, Y. Chen, L. Wang, Nitrogen-doped carbon nanotubes as efficient and durable metal-free cathodic catalysts for oxygen reduction in microbial fuel cells, Energy Environ. Sci. 4 (2011) 1892–1899.

[21] Z. Fan, J. Li, Y. Zhou, Q. Fu, W. Yang, X. Zhu, Q. Liao, A green, cheap, high-performance carbonaceous catalyst derived from Chlorella pyrenoidosa for oxygen reduction reaction in microbial fuel cells, Int J Hydrogen Energ 42 (2017) 27657–27665.

[22] Z.Q. Liu, H. Cheng, N. Li, T.Y. Ma, Y.Z. Su, ZnCo2O4 quantum dots anchored on nitrogen-doped carbon nanotubes as reversible oxygen reduction/evolution electrocatalysts, Adv. Mater. 28 (2016) 3777–3784.

[23] Z.L. Li, G.L. Li, L.H. Jiang, J.L. Li, G.Q. Sun, C.G. Xia, F.W. Li, Ionic liquids as precursors for efficient mesoporous Iron-nitrogen-doped oxygen reduction electrocatalysts, Angew Chem Int Edit 54 (2015) 1494–1498.

[24] X.-X. Ma, X.-Q. He, T. Asefa, Hierarchically porous Co3C/Co-NC/G modified graphitic carbon: a trifunctional corrosion-resistant electrode for oxygen reduction, hydrogen evolution and oxygen evolution reactions, Electrochim. Acta 257 (2017) 40–48.

[25] Y.J. Sa, D.J. Seo, J. Woo, J.T. Lim, J.Y. Cheon, S.Y. Yang, J.M. Lee, D. Kang, T.J. Shin, H.S. Shin, H.Y. Jeong, C.S. Kim, M.G. Kim, T.Y. Kim, S.H. Joo, A general approach to preferential formation of active Fe-N-x sites in Fe/N/C electrocatalysts for efficient oxygen reduction reaction, J. Am. Chem. Soc. 138 (2016) 15046–15056.

[26] H. Yu, L. Shang, T. Bian, R. Shi, G.I. Waterhouse, Y. Zhao, C. Zhou, L.Z. Wu, C.H. Tung, T. Zhang, Nitrogen-doped porous carbon nanosheets templated from g-C3N4 as metal-free electrocatalysts for efficient oxygen reduction reaction, Adv. Mater. 28 (2016) 5080–5086.

[27] Y. Peng, B.Z. Lu, L.M. Chen, N. Wang, J.E. Lu, Y. Ping, S.W. Chen, Hydrogen evolution reaction catalyzed by ruthenium ion-complexed graphitic carbon nitride nanosheets, J. Mater. Chem. A 5 (2017) 18261–18269.

[28] Y. Peng, W.Z. Pan, N. Wang, J.E. Lu, S.W. Chen, Ruthenium ion-complexed graphitic carbon nitride nanosheets supported on reduced graphene oxide as high-performance catalysts for electrochemical hydrogen evolution, Chemsuschem 11 (2018) 130–136.

[29] W. Yang, Y. Peng, Y.D. Zhang, J.E. Lu, J. Li, S.W. Chen, Air cathode catalysts of microbial fuel cell by nitrogen-doped carbon aerogels, ACS Sustain. Chem. Eng. 7 (2019) 3917–3924.

[30] Z. Mo, S. Liao, Y. Zheng, Z. Fu, Preparation of nitrogen-doped carbon nanotube arrays and their catalysis towards cathodic oxygen reduction in acidic and alkaline media, Carbon 50 (2012) 2620–2627.

[31] B.G. Sumpter, J. Huang, V. Meunier, J.M. Romo-Herrera, E. Cruz-Silva, H. Terrones, M. Terrones, A theoretical and experimental study on manipulating the structure and properties of carbon nanotubes using substitutional dopants, Int. J. Quantum Chem. 109 (2009) 97–118.

[32] P.G. Hu, P. Liu, C.P. Deming, S.W. Chen, Multifunctional graphene-based nanostructures for efficient electrocatalytic reduction of oxygen, J. Chem. Technol. Biotechnol. 90 (2015) 2132–2151.

[33] H.S. Lu, H.M. Zhang, R.R. Liu, X. Zhang, H.J. Zhao, G.Z. Wang, Macroscale cobalt-MOFs derived metallic co nanoparticles embedded in N-doped porous carbon layers as efficient oxygen electrocatalysts, Appl. Surf. Sci. 392 (2017) 402–409.

[34] A.N. Pour, E. Hosaini, A. Tavasoli, A. Behroozsarand, F. Dolati, Intrinsic kinetics of Fischer Tropsch synthesis over Co/CNTs catalyst: effects of metallic cobalt particle size, J Nat Gas Sci Eng 21 (2014) 772–778.

[35] W.L. Yao, J.Q. Chen, H.W. Cheng, Platelike CoO/carbon nanofiber composite electrode with improved electrochemical performance for lithium ion batteries, J. Solid State Electrochem. 15 (2011) 183–188.

[36] I. Papailias, T. Giannakopoulou, N. Todorova, D. Demotikali, T. Vaimakis, C. Trapalis, Effect of processing temperature on structure and photocatalytic properties of g-C3N4, Appl. Surf. Sci. 358 (2015) 278–286.

[37] J. Wang, H. Wu, D. Gao, S. Miao, G. Wang, X. Bao, High-density iron nanoparticles encapsulated within nitrogen-doped carbon nanoshell as efficient oxygen electrocatalyst for zinc–air battery, Nano Energy 13 (2015) 387–396.

[38] G. Xu, G.C. Xu, J.J. Ban, L. Zhang, H. Lin, C.L. Qi, Z.P. Sun, D.Z. Jia, Cobalt and cobalt oxides N-codoped porous carbon derived from metal-organic framework as bifunctional catalyst for oxygen reduction and oxygen evolution reactions, J Colloid Interf Sci 521 (2018) 141–149.

[39] A. Gabe, J. Garcia-Aguilar, A. Berenguer-Murcia, E. Morallon, D. Cazorla-Amoros, Key factors improving oxygen reduction reaction activity in cobalt nanoparticles modified carbon nanotubes, Appl Catal B-Environ 217 (2017) 303–312.

[40] B. Erable, L. Etcheverry, A. Bergel, Increased power from a two-chamber microbial fuel cell with a low-pH air-cathode compartment, Electrochem. Commun. 11 (2009) 619–622.

[41] O. Istanbullu, J. Babauta, H.D. Nguyen, H. Beyenal, Electrochemical biofilm control: mechanism of action, Biofouling 28 (2012) 769–778.

[42] T. Kim, J. An, H. Lee, J.K. Jang, I.S. Chang, pH-dependent ammonia removal pathways in microbial fuel cell system, Bioresour. Technol. 215 (2016) 290–295.

[43] M. Oliot, S. Galier, H.R. de Balmann, A. Bergel, Ion transport in microbial fuel cells: key roles, theory and critical review, Appl. Energy 183 (2016) 1682–1704.

[44] S.C. Popat, D. Ki, B.E. Rittmann, C.I. Torres, Importance of OH− transport from cathodes in microbial fuel cells, Chemsuschem 5 (2012) 1071–1079.

[45] Y. Yuan, S. Zhou, J. Tang, In situ investigation of cathode and local biofilm microenvironments reveals important roles of OH–and oxygen transport in microbial fuel cells, Environ Sci Technol 47 (2013) 4911–4917.